

Article

Incompatibility Stresses and Lattice Rotations Due to Grain Boundary Sliding in Heterogeneous Anisotropic Elasticity

Thiebaud Richeton

Laboratoire d'Etude des Microstructures et de Mécanique des Matériaux (LEM3), UMR 7239, CNRS/Université de Lorraine, 7 rue Félix Savart, 57073 Metz, France; thiebaud.richeton@univ-lorraine.fr

Academic Editor: Sinisa Dj. Mesarovic

Received: 29 April 2017; Accepted: 26 June 2017; Published: 4 July 2017

Abstract: Non-uniform grain boundary sliding can induce strain and rotation incompatibilities at perfectly planar interfaces. Explicit analytic expressions of stress and lattice rotation jumps are thus derived at a planar interface in the general framework of heterogeneous anisotropic thermo-elasticity with plasticity and grain boundary sliding. Both elastic fields are directly dependent on in-plane gradients of grain boundary sliding. It is also shown that grain boundary sliding is a mechanism that may relax incompatibility stresses of elastic, plastic and thermal origin although the latter are not resolved on the grain boundary plane. This relaxation may be a driving force for grain boundary sliding in addition to the traditionally considered local shears on the grain boundary plane. Moreover, the obtained analytic expressions are checked by different kinds of bicrystal shearing finite element simulations allowing grain boundary sliding and where a pinned line in the interface plane aims at representing the effect of a triple junction. A very good agreement is found between the analytic solutions and the finite element results. The performed simulations particularly emphasize the role of grain boundary sliding as a possible strong stress generator around the grain boundary close to the triple line because of the presence of pronounced gradients of sliding.

Keywords: grain boundary sliding; incompatibility stresses; anisotropic elasticity; heterogeneous elasticity; lattice rotations

1. Introduction

Grain boundary sliding (GBS) is a specific deformation mechanism of polycrystals which is especially important during creep [1–6]. While GBS can act as a stress relaxation mechanism able to lead to superplasticity, it may also induce cavities at triple points and causes intergranular fracture initiation [3,6–8]. GBS generally needs relatively high homologous temperature and/or relatively small grain sizes [1–4]. However, it is also sometimes observed with coarse grain sizes at room temperature, particularly in metals with hexagonal close-packed (HCP) structure [5–7,9,10]. Due to the low symmetry of the hexagonal lattice, HCP materials are known to be strongly anisotropic and thus to exhibit significant strain incompatibilities between adjacent grains. In those materials, the origin of GBS might hence be the need for an additional mechanism that can accommodate grain incompatibilities [6,7,9].

Some years ago, Mussot et al. [7] derived compatibility conditions at sliding smooth interfaces which showed that GBS modifies strain compatibility conditions as soon as GBS is non-uniform. The relevancy of this result is reinforced by the many experimental evidences indicating that sliding is usually non-uniform along a grain boundary [6,7,9]. Hence, gradients of GBS can induce or relax internal stresses. It must be noticed that the strain incompatibilities of which the study of Mussot et al. [7] referred to are different from the ones generated by uniform gliding of rough interfaces

that are believed to control the rate at which GBS occurs [2] or the ones created at triple points that require accommodating processes like migration of the triple edges, diffusion along grain boundaries or dislocation activity in the neighboring grains [3].

The present paper follows the work of Mussot et al. [7] in order to extend strain compatibility conditions at a sliding interface, assumed perfectly planar, to the general context of heterogeneous anisotropic thermo-elasticity with plastic distortions. Moreover, explicit analytic expressions of incompatibility stresses and lattice rotations are looked for. The correctness of the obtained solutions are checked thanks to finite elements (FE) simulations of bicrystals shearing. In the grain boundary plane, a line is pinned in order to mimic the effect of a triple junction. Based on both the obtained theoretical expressions and numerical results, the dual role of grain boundary sliding, as a stress generator and as a stress relaxation mechanism, is then discussed.

Notation and Reduction Conventions

A vector is denoted $\underline{x} \equiv x_i$, a second-order tensor $\underline{X} \equiv X_{ij}$ and a fourth-order tensor $\underline{\underline{X}} \equiv X_{ijkl}$. The Einstein summation convention over repeated indices is used. The symbol $\underline{\underline{A}} : \underline{\underline{B}}$ represents tensor multiplication, $\underline{\underline{A}} :$ the contracted product between two tensors and ∇ , div and $curl$ the gradient, divergence and curl operators, respectively. In rectangular Cartesian coordinates, we have in particular:

$$\underline{\underline{A}} \cdot \underline{b} \equiv A_{ij}b_j, \quad (1)$$

$$\underline{\underline{A}} : \underline{\underline{B}} \equiv A_{ijkl}B_{kl}, \quad (2)$$

$$(\nabla \underline{X})_{ij} = X_{i,j}, \quad (3)$$

$$(div \underline{X})_i = X_{ij,j}, \quad (4)$$

$$(curl \underline{\underline{X}})_{ij} = \epsilon_{jlm} X_{im,l}, \quad (5)$$

where ϵ_{jlm} is a component of the third-order alternating Levi-Civita tensor. The jump of a mechanical or material property field f at an interface between two crystals I and II which is oriented by \underline{x}_2 is noted $[[f]]$ such that $[[f]] = f^{II}(x_2 \rightarrow 0^+) - f^I(x_2 \rightarrow 0^-)$, whereas the average of f across the interface is defined as $\hat{f} = \frac{1}{2}(f^I(x_2 \rightarrow 0^-) + f^{II}(x_2 \rightarrow 0^+))$.

Finally, the contracted Voigt notation [11] ($11 \rightarrow 1, 22 \rightarrow 2, 33 \rightarrow 3, 23 \rightarrow 4, 31 \rightarrow 5, 12 \rightarrow 6$) is adopted in Section 2.2. The contracted product between tensors $\underline{\underline{A}}$ and $\underline{\underline{B}}$ is then written as $(\underline{\underline{A}} : \underline{\underline{B}})_p = A_{pq}B_q$ where p and q take values ranging from 1 to 6. For consistency, an engineering convention is considered for strain components, i.e., $\epsilon_4 = 2\epsilon_{23}, \epsilon_5 = 2\epsilon_{31}, \epsilon_6 = 2\epsilon_{12}$, and the Hooke's law in matrix notation is given as:

$$\begin{bmatrix} \epsilon_1^e \\ \epsilon_2^e \\ \epsilon_3^e \\ \epsilon_4^e \\ \epsilon_5^e \\ \epsilon_6^e \end{bmatrix} = \begin{bmatrix} s_{11} & s_{12} & s_{13} & s_{14} & s_{15} & s_{16} \\ s_{12} & s_{22} & s_{23} & s_{24} & s_{25} & s_{26} \\ s_{13} & s_{23} & s_{33} & s_{34} & s_{35} & s_{36} \\ s_{14} & s_{24} & s_{34} & s_{44} & s_{45} & s_{46} \\ s_{15} & s_{25} & s_{35} & s_{45} & s_{55} & s_{56} \\ s_{16} & s_{26} & s_{36} & s_{46} & s_{56} & s_{66} \end{bmatrix} \begin{bmatrix} \sigma_1 \\ \sigma_2 \\ \sigma_3 \\ \sigma_4 \\ \sigma_5 \\ \sigma_6 \end{bmatrix} \quad (6)$$

where σ_i are stresses, ϵ_i^e elastic strains and s_{ij} components of the elastic compliances tensor that include the multiplying factors of 2 and 4 [11].

2. Analytical Derivation of Elastic Field Jumps

2.1. Compatibility Relations

In a continuous medium of infinite volume V , an infinite planar grain boundary (GB) is considered which separates two crystals I and II (Figure 1). The unit vector \underline{n} designates the normal to the interface

and is assumed to be oriented from crystal *I* towards crystal *II* along the direction \underline{x}_2 (Figure 1). In what follows, superscripts *I* and *II* correspond to crystals *I* ($x_2 < 0$) and *II* ($x_2 > 0$), respectively. This bicrystal is supposed to have been deformed under the action of homogenous macroscopic mechanical loading applied on the external boundary ∂V of V and of homogeneous temperature variation ΔT and in the absence of body forces. Elasticity, plasticity and GBS are considered as deformation mechanisms in a static small strain setting. It is assumed that the elastic compliance tensor $\underline{\underline{s}}$ and the symmetric thermal expansion tensor $\underline{\underline{\alpha}}^T$ are isotherm and uniform in each crystal and that the plastic distortion tensor $\underline{\underline{\beta}}^p$ depends only on x_2 :

$$\underline{\underline{s}} = \underline{\underline{s}}^I + \llbracket \underline{\underline{s}} \rrbracket H(x_2), \tag{7}$$

$$\underline{\underline{\alpha}}^T = \underline{\underline{\alpha}}^{T I} + \llbracket \underline{\underline{\alpha}}^T \rrbracket H(x_2), \tag{8}$$

$$\underline{\underline{\beta}}_{,1}^p = \underline{\underline{\beta}}_{,3}^p = \underline{\underline{0}}, \tag{9}$$

where $H(x_2)$ is the Heaviside unit step function. GBS is described through the distortion tensor $\underline{\underline{\beta}}^S$. Similarly to the expression of the plastic distortion tensor induced by the formation of a dislocation loop [12,13], $\underline{\underline{\beta}}^S$ is singular on the interface and, for a GB with unit normal $\underline{n} \equiv \underline{x}_2$, may be expressed as:

$$\beta_{ij}^S = g_i(x_1, x_3) \delta_{j2} \delta(x_2), \tag{10}$$

where the vector \underline{g} represents the jump of displacement \underline{u} at the interface due to sliding:

$$\underline{g} = \llbracket \underline{u} \rrbracket. \tag{11}$$

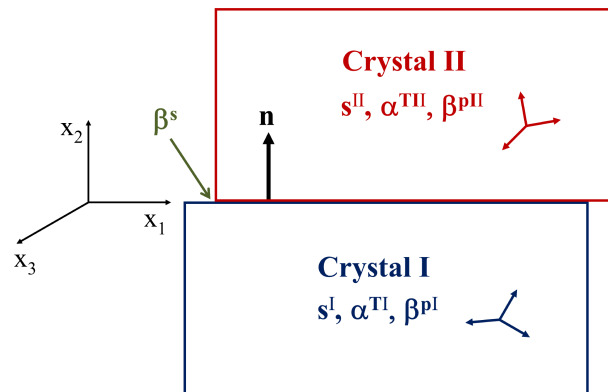


Figure 1. Infinite planar grain boundary exhibiting GBS (see text for notations).

Moreover, considering the absence of interface decohesion implies $g_2 = 0$ [7]. The only non-zero components of $\underline{\underline{\beta}}^S$ are thus β_{12}^S and β_{32}^S . As a consequence of all the preceding assumptions, the total distortion $\underline{\underline{\beta}}$ may be written as follows:

$$\beta_{ij}(x_1, x_2, x_3) = \beta_{ij}^e(x_1, x_2, x_3) + \beta_{ij}^p(x_2) + \left(\alpha_{ij}^{T I} + \llbracket \alpha_{ij}^T \rrbracket H(x_2) \right) \Delta T + g_i(x_1, x_3) \delta_{j2} \delta(x_2), \tag{12}$$

with $\underline{\underline{\beta}}^e$ the elastic distortion tensor. According to the orthogonal Stokes-Helmholtz decomposition [14–16], it is possible to decompose $\underline{\underline{\beta}}^e$ into compatible and incompatible parts:

$$\tilde{\beta}^e = \tilde{\beta}_{\parallel}^e + \tilde{\beta}_{\perp}^e, \quad (13)$$

such as:

$$\text{curl } \tilde{\beta}_{\parallel}^e = 0 \text{ and } \text{div } \tilde{\beta}_{\perp}^e = 0. \quad (14)$$

In order to ensure the unicity of this decomposition, the following condition is considered on ∂V [14–16]:

$$\tilde{\beta}_{\perp}^e \cdot \underline{m} = 0, \quad (15)$$

where \underline{m} is the unit normal of ∂V . As a consequence of this decomposition, the Nye tensor $\tilde{\alpha}$ [17] (or dislocation density tensor), which may be defined as the curl of the elastic distortion [14], can be written solely from the incompatible part of the elastic distortion:

$$\tilde{\alpha} = \text{curl } \tilde{\beta}^e = \text{curl } \tilde{\beta}_{\perp}^e. \quad (16)$$

As a result of Equations (14)–(16), $\tilde{\beta}_{\perp}^e$ is thus given as the unique solution of the following Poisson equation:

$$\begin{cases} \Delta \tilde{\beta}_{\perp}^e = -\text{curl } \tilde{\alpha} \\ \tilde{\beta}_{\perp}^e \cdot \underline{n} = 0 \text{ on } \partial V. \end{cases} \quad (17)$$

Then, by considering the compatibility of the total distortion ($\text{curl } \tilde{\beta} = 0$), Equations (12) and (16) lead to:

$$\alpha_{ij} = -\epsilon_{j2m} \left(\beta_{im,2}^p + \llbracket \alpha_{im}^T \rrbracket \Delta T \delta(x_2) \right) - \epsilon_{j12} g_{i,l} \delta(x_2). \quad (18)$$

By making the additional hypothesis that the gradients $g_{i,l}$ are uniform, $\tilde{\alpha}$ depends only on x_2 . The same is true for $\tilde{\beta}_{\perp}^e$ since it is given as the unique solution of the Poisson Equation (17). Hence, it is possible to write the elastic distortion as:

$$\tilde{\beta}^e = \nabla \underline{z} + \tilde{\beta}_{\perp}^e(x_2), \quad (19)$$

where \underline{z} is a continuous vector such as $\nabla \underline{z} = \tilde{\beta}_{\parallel}^e$ [14–16]. From relation (19), we have then:

$$\forall j \neq 2, \beta_{i2,j}^e = z_{i,2j} = z_{i,j2}. \quad (20)$$

By considering again the compatibility of the total distortion, we can write:

$$\forall i \neq 2, \forall j \neq 2, \beta_{ij,2} - \beta_{i2,j} = 0. \quad (21)$$

Combining this relation with Equations (12) and (20), we obtain:

$$\forall i \neq 2, \forall j \neq 2, \beta_{ij,2}^e = z_{i,j2} - \beta_{ij,2}^p - \left(\llbracket \alpha_{ij}^T \rrbracket \Delta T - g_{i,j} \right) \delta(x_2) = 0, \quad (22)$$

which becomes by integration with respect to x_2 :

$$\forall i \neq 2, \forall j \neq 2, \beta_{ij}^e = z_{i,j} - \beta_{ij}^p - \left(\llbracket \alpha_{ij}^T \rrbracket \Delta T - g_{i,j} \right) H(x_2) + K_{ij}, \quad (23)$$

where K_{ij} are spatially uniform constants. By definition, we have $\llbracket z_i \rrbracket = 0$, thus $\forall j \neq 2, \llbracket z_{i,j} \rrbracket = 0$ and accordingly:

$$\forall i \neq 2, \forall j \neq 2, \llbracket \beta_{ij}^e \rrbracket = -\llbracket \beta_{ij}^p \rrbracket - \llbracket \alpha_{ij}^T \rrbracket \Delta T + g_{i,j}. \quad (24)$$

These relations are in agreement with the compatibility relations derived by Mussot et al. [7]. They show that GBS can induce strain and rotation incompatibilities as soon as the sliding is non-uniform. The terms $g_{i,j(j \neq 2)}$ are indeed directly related to the gradients of β_{12}^S and β_{32}^S according to the relations:

$$\begin{aligned}\forall j \neq 2, \beta_{12,j}^S &= g_{1,j} \delta(x_2), \\ \forall j \neq 2, \beta_{32,j}^S &= g_{3,j} \delta(x_2).\end{aligned}\quad (25)$$

2.2. Stress Jumps

Using the contracted notation of Voigt [11], relation (24) makes it possible to write the following system:

$$\begin{aligned}[\varepsilon_1^e] &= [s_{1j} \sigma_j] = -[\varepsilon_1^p] - [\alpha_1^T] \Delta T + (\nabla^S g)_1, \\ [\varepsilon_3^e] &= [s_{3j} \sigma_j] = -[\varepsilon_3^p] - [\alpha_3^T] \Delta T + (\nabla^S g)_3, \\ [\varepsilon_5^e] &= [s_{5j} \sigma_j] = -[\varepsilon_5^p] - [\alpha_5^T] \Delta T + (\nabla^S g)_5,\end{aligned}\quad (26)$$

where $\nabla^S g$ is the symmetrized gradient of g . The same engineering convention as for strain components is considered, i.e., $(\nabla^S g)_5 = g_{1,3} + g_{3,1}$. Considering the continuity of the traction vector at the boundary, $[\underline{\sigma} \cdot \underline{n}] = 0$, and using the relation $[\underline{s} : \underline{\sigma}] = [\underline{s}] : \hat{\underline{\sigma}} + \hat{\underline{s}} : [\underline{\sigma}]$, the system (26) becomes:

$$\begin{aligned}\hat{s}_{11} [\sigma_1] + \hat{s}_{13} [\sigma_3] + \hat{s}_{15} [\sigma_5] &= -[s_{1j}] \hat{\sigma}_j - [\varepsilon_1^p] - [\alpha_1^T] \Delta T + (\nabla^S g)_1, \\ \hat{s}_{13} [\sigma_1] + \hat{s}_{33} [\sigma_3] + \hat{s}_{35} [\sigma_5] &= -[s_{3j}] \hat{\sigma}_j - [\varepsilon_3^p] - [\alpha_3^T] \Delta T + (\nabla^S g)_3, \\ \hat{s}_{15} [\sigma_1] + \hat{s}_{35} [\sigma_3] + \hat{s}_{55} [\sigma_5] &= -[s_{5j}] \hat{\sigma}_j - [\varepsilon_5^p] - [\alpha_5^T] \Delta T + (\nabla^S g)_5.\end{aligned}\quad (27)$$

By introducing the notation:

$$[\underline{\varepsilon}^*] = [\underline{s}] : \hat{\underline{\sigma}} + [\underline{\varepsilon}^p] + [\underline{\alpha}^T] \Delta T - \nabla^S g, \quad (28)$$

the system (27) becomes similar to the one obtained for the derivation of incompatibility stresses without GBS and thermal expansion in bicrystals or periodic-layered composites [18–20]. Therefore, stress jumps solutions can be directly expressed as:

$$[\underline{\sigma}] = \underline{\underline{G}} : [\underline{\varepsilon}^*], \quad (29)$$

where the non-zero components of the tensor $\underline{\underline{G}}$ are given by [19,20]:

$$\begin{aligned}G_{11} &= (\hat{s}_{33} \hat{s}_{55} - \hat{s}_{35}^2) / D, & G_{13} &= G_{31} = (\hat{s}_{15} \hat{s}_{35} - \hat{s}_{13} \hat{s}_{55}) / D, \\ G_{33} &= (\hat{s}_{11} \hat{s}_{55} - \hat{s}_{15}^2) / D, & G_{15} &= G_{51} = (\hat{s}_{13} \hat{s}_{35} - \hat{s}_{15} \hat{s}_{33}) / D, \\ G_{55} &= (\hat{s}_{11} \hat{s}_{33} - \hat{s}_{13}^2) / D, & G_{35} &= G_{53} = (\hat{s}_{13} \hat{s}_{15} - \hat{s}_{35} \hat{s}_{11}) / D,\end{aligned}\quad (30)$$

with $D = \hat{s}_{11} \hat{s}_{35}^2 + \hat{s}_{33} \hat{s}_{15}^2 + \hat{s}_{55} \hat{s}_{13}^2 - \hat{s}_{11} \hat{s}_{33} \hat{s}_{55} - 2 \hat{s}_{13} \hat{s}_{15} \hat{s}_{35}$.

Equations (28)–(30) show that incompatibility stresses are directly dependent on in-plane gradients of GBS. It is seen that GBS is a mechanism capable of relaxing incompatibility stresses of elastic, plastic and thermal origin although the latter are not resolved on the grain boundary plane. This relaxation may be a driving force for GBS in addition to the traditionally considered local shears on the grain boundary plane.

It is noteworthy than the expressions of the stress jumps are much simpler if ones considers isotropic homogeneous thermo-elasticity properties [18]. With μ the shear modulus and ν the Poisson's ratio, the expressions of the non-zero stress jump components are indeed written in this case as:

$$\begin{aligned} \llbracket \sigma_1 \rrbracket &= -\frac{2\mu}{1-\nu} \left(\llbracket \varepsilon_1^p \rrbracket + \nu \llbracket \varepsilon_3^p \rrbracket - \left(\nabla^S g \right)_1 - \nu \left(\nabla^S g \right)_3 \right) \\ \llbracket \sigma_3 \rrbracket &= -\frac{2\mu}{1-\nu} \left(\llbracket \varepsilon_3^p \rrbracket + \nu \llbracket \varepsilon_1^p \rrbracket - \left(\nabla^S g \right)_3 - \nu \left(\nabla^S g \right)_1 \right) \\ \llbracket \sigma_5 \rrbracket &= -\mu \left(\llbracket \varepsilon_5^p \rrbracket - \left(\nabla^S g \right)_5 \right). \end{aligned} \quad (31)$$

2.3. Lattice Rotation Jumps

From relation (24), the jumps of elastic rotation in presence of GBS may expressed as:

$$\begin{aligned} \llbracket \omega_{32}^e \rrbracket &= \llbracket \varepsilon_{23}^e \rrbracket + \llbracket \beta_{23}^p \rrbracket + \llbracket a_{23}^T \rrbracket \Delta T, \\ \llbracket \omega_{13}^e \rrbracket &= -\llbracket \omega_{13}^p \rrbracket + \frac{1}{2} (g_{1,3} - g_{3,1}), \\ \llbracket \omega_{21}^e \rrbracket &= -\llbracket \varepsilon_{12}^e \rrbracket - \llbracket \beta_{21}^p \rrbracket - \llbracket a_{12}^T \rrbracket \Delta T, \end{aligned} \quad (32)$$

with $\llbracket \varepsilon^e \rrbracket = \llbracket \underline{\underline{s}} \rrbracket : \hat{\sigma} + \hat{\underline{\underline{s}}} : \llbracket \sigma \rrbracket$. All the components of the lattice rotation tensor hence depend on the in-plane gradients of GBS, which shows the influence of GBS on the evolution of crystallographic textures [21]. It can be noticed that in case of homogenous isotropic elastic properties, we have $\llbracket \varepsilon_{23}^e \rrbracket = \llbracket \varepsilon_{12}^e \rrbracket = 0$.

3. Validation by FE Simulations

The correctness of the analytic formulas (28)–(32) are checked thanks to FE simulations performed with the software ABAQUS/standard. Two rectangular grains, α and β , of dimensions $120 \times 90 \times 60$ are defined as two different parts (Figure 2) and discretized into a regular mesh made of 173972 8-node linear brick elements (C3D8). The initial position of the upper face of the first grain matches exactly the position of the bottom face of the second grain and corresponds to $x_2 = 0$. The behavior is supposed to be purely elastic (no plasticity, no thermal expansion) with a possibility of GBS. Zn which has a HCP structure is considered as a reference material. The crystallographic orientations of the two grains are indicated in Figure 3. Six different simulations are performed. They have in common that the top ($x_2 = 90$) and bottom ($x_2 = -90$) faces are constrained to be planar ($u_2 = \text{constant}$), that the continuity of u_2 is enforced at the GB ($\llbracket u_2 \rrbracket = 0$) and that the line at $x_1 = -60$ and $x_2 = 0$ is pinned ($u_1 = u_2 = u_3 = 0$) (Figure 2). This pinned line may represent a fixed GB junction like a triple line and aims to produce GBS gradients. In order to induce an effective contact between the two parts, a very small compression ($\varepsilon_{22} = 10^{-6}$) is applied on the bicrystal external boundary in a first time step for all the simulations. Then, the following additional boundary and interface conditions are applied during a second time step of 1 s:

- Simulation 1: $\dot{u}_1 = 10^{-3} \text{s}^{-1}$ on the top face, $\dot{u}_1 = -10^{-3} \text{s}^{-1}$ on the bottom face, grain α at the bottom ($x_2 < 0$) and $\llbracket u_1 \rrbracket = \llbracket u_3 \rrbracket = 0$ (no GBS allowed),
- Simulation 2: $\dot{u}_1 = 10^{-3} \text{s}^{-1}$ on the top face, $\dot{u}_1 = -10^{-3} \text{s}^{-1}$ on the bottom face, grain α at the bottom ($x_2 < 0$), $\llbracket u_3 \rrbracket = 0$ and $\llbracket u_1 \rrbracket \neq 0$ (β_{12}^S allowed),
- Simulation 3: $\dot{u}_1 = 10^{-3} \text{s}^{-1}$ on the top face, $\dot{u}_1 = -10^{-3} \text{s}^{-1}$ on the bottom face, grain α at the top ($x_2 > 0$), $\llbracket u_3 \rrbracket = 0$ and $\llbracket u_1 \rrbracket \neq 0$ (β_{12}^S allowed),
- Simulation 4: $\dot{u}_3 = 10^{-3} \text{s}^{-1}$ on the top face, $\dot{u}_3 = -10^{-3} \text{s}^{-1}$ on the bottom face, grain α at the bottom ($x_2 < 0$) and $\llbracket u_1 \rrbracket = \llbracket u_3 \rrbracket = 0$ (no GBS allowed),
- Simulation 5: $\dot{u}_3 = 10^{-3} \text{s}^{-1}$ on the top face, $\dot{u}_3 = -10^{-3} \text{s}^{-1}$ on the bottom face, grain α at the bottom ($x_2 < 0$), $\llbracket u_1 \rrbracket = 0$ and $\llbracket u_3 \rrbracket \neq 0$ (β_{32}^S allowed),

- Simulation 6: $\dot{u}_3 = 10^{-3}\text{s}^{-1}$ on the top face, $\dot{u}_3 = -10^{-3}\text{s}^{-1}$ on the bottom face, grain α at the top ($x_2 > 0$), $[[u_1]] = 0$ and $[[u_3]] \neq 0$ (β_{32}^S allowed),

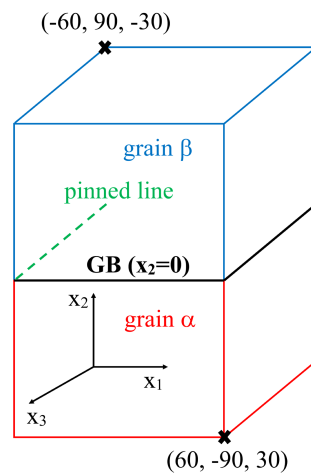


Figure 2. Sketch of the two rectangular grains of dimensions $120 \times 90 \times 60$ used for the FE simulations. The line at $x_1 = -60$ and $x_2 = 0$ is pinned ($u_1 = u_2 = u_3 = 0$).

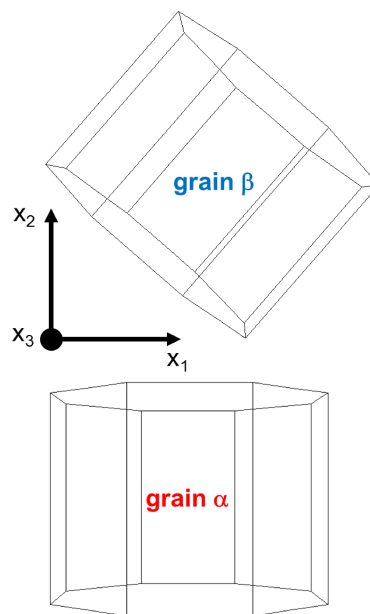


Figure 3. Orientation of the hexagonal cell for the two grains. Their orientations correspond to $[0001]_{(C)} \parallel [010]_{(G)}$ and $[10\bar{1}0]_{(C)} \parallel [001]_{(G)}$ for grain α and $[0001]_{(C)} \parallel [670]_{(G)}$ and $[10\bar{1}0]_{(C)} \parallel [7\bar{6}0]_{(G)}$ for grain β , with (C) the crystal frame and (G) the global frame.

A classical crystal-elasticity UMAT subroutine is used to compute the displacements and the stresses (see for e.g., [18]). In these simulations, when GBS is allowed, it is completely free to develop (no friction, no critical stress), which corresponds to an extreme, not realistic, situation. Figures 4 and 5 show the profiles of $g_1 = [[u_1]]$ and $g_3 = [[u_3]]$ along x_1 at $x_3 = 0$ for simulations 2, 3 and 5, 6, respectively. The values of g_i must be appreciated with respect to the dimensions of the bicrystal ($120 \times 90 \times 60$). It can be noticed that a maximum value around 0.5 is reached in the four simulations, which corresponds to a shear strain of about 0.3%. Furthermore, it has been checked that considering sliding with isotropic Coulomb friction keep the profiles of g_i similar with however lower saturation values.

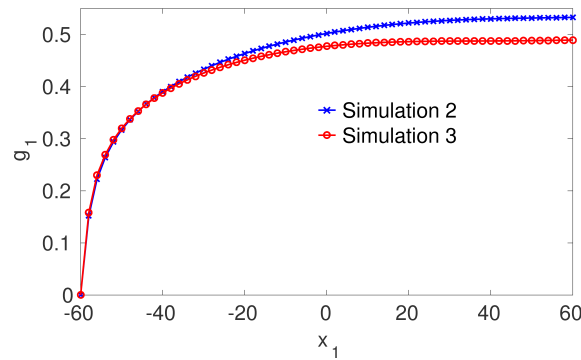


Figure 4. Profiles of $g_1 = \llbracket u_1 \rrbracket$ along x_1 at $x_3 = 0$ for simulations 2 and 3.

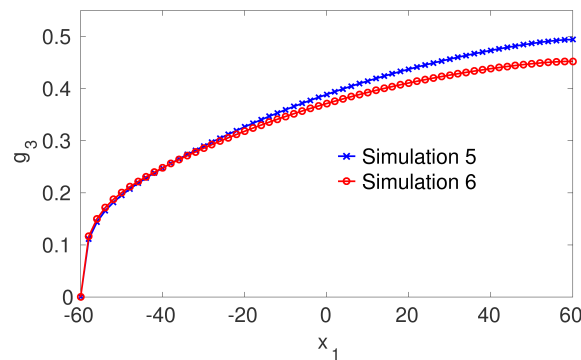


Figure 5. Profiles of $g_3 = \llbracket u_3 \rrbracket$ along x_1 at $x_3 = 0$ for simulations 5 and 6.

Comparisons of the analytic formulas (28)–(30) and (32) with results of the FE simulations are performed at three different points: $A(-40, 0, 0)$, $B(0, 0, 0)$ and $C(40, 0, 0)$ (Tables 1–6). The analytic formulas are computed thanks to a numerical code based on the software package Matlab (R2015a). The input parameters of this code are the elastic properties of Zn given in Table 7, the crystallographic orientations of the two grains and the component values of $\hat{\sigma}$ and $\nabla \underline{g}$ which are directly collected from the FE simulation results (Tables 1–6). Besides, Figures 6–11 display profiles of Von Mises stress along x_2 through points A, B and C obtained by the different FE simulations.

Table 1. Values of $\hat{\sigma}$ (MPa) provided by the FE simulation 1 and used to compute the analytic formulas (28)–(30) and (32) (top). Comparisons of the values of $\llbracket \underline{\sigma} \rrbracket$ (MPa) and $\llbracket \omega^e \rrbracket$ ($^\circ$) given by the FE simulation 1 and those computed from the analytic formulas (bottom).

	A (−40, 0, 0)	B (0, 0, 0)	C (40, 0, 0)
$\hat{\sigma}_{11}$	−42.2	−18.4	5.2
$\hat{\sigma}_{22}$	−38.5	−30.5	32.6
$\hat{\sigma}_{33}$	−6.9	−3.6	3.5
$\hat{\sigma}_{23}$	0.0	0.0	0.0
$\hat{\sigma}_{31}$	0.0	0.0	0.0
$\hat{\sigma}_{12}$	35.2	77.6	61.0
	FE/Analytic	FE/Analytic	FE/Analytic
$\llbracket \sigma_{11} \rrbracket$	11.6/6.8	−34.9/−34.5	−66.3/−68.5
$\llbracket \sigma_{33} \rrbracket$	37.1/32.2	72.4/73.0	38.2/37.5
$\llbracket \sigma_{31} \rrbracket$	0.0/0.0	0/0	0.0/0.0
$\llbracket \omega_{32}^e \rrbracket$	0.00/0.00	0.00/0.00	0.00/0.00
$\llbracket \omega_{13}^e \rrbracket$	0.00/0.00	0.00/0.00	0.00/0.00
$\llbracket \omega_{21}^e \rrbracket$	0.00/0.00	−0.03/−0.05	−0.04/−0.08

Table 2. Values of $\hat{\sigma}$ (MPa) and ∇g provided by the FE simulation 2 and used to compute the analytic formulas (28)–(30) and (32) (top). Comparisons of the values of $[[\sigma]]$ (MPa) and $[[\omega^e]]$ (°) given by the FE simulation 2 and those computed from the analytic formulas (bottom).

	A (−40, 0, 0)	B (0, 0, 0)	C (40, 0, 0)
$g_{1,1}$	0.00532	0.00139	0.00021
$g_{1,3}$	0.00000	0.00000	0.00000
$\hat{\sigma}_{11}$	−28.4	2.0	4.8
$\hat{\sigma}_{22}$	−9.2	−2.3	16.3
$\hat{\sigma}_{33}$	27.7	−3.6	−2.9
$\hat{\sigma}_{23}$	0.0	0.0	0.0
$\hat{\sigma}_{31}$	0.0	0.0	0.0
$\hat{\sigma}_{12}$	11.4	2.3	1.0
	FE / Analytic	FE / Analytic	FE / Analytic
$[[\sigma_{11}]]$	592.0/598.9	150.5/151.5	10.0/9.4
$[[\sigma_{33}]]$	67.9/77.8	21.1/22.8	−1.8/−2.4
$[[\sigma_{31}]]$	0.0/0.0	0/0.0	0.0/0.0
$[[\omega_{32}^e]]$	0.00/0.00	0.00/0.00	0.00/0.00
$[[\omega_{13}^e]]$	0.00/0.00	0.00/0.00	0.00/0.00
$[[\omega_{21}^e]]$	−0.05/−0.10	−0.02/−0.03	−0.01/−0.01

Table 3. Values of $\hat{\sigma}$ (MPa) and ∇g provided by the FE simulation 3 and used to compute the analytic formulas (28)–(30) and (32) (top). Comparisons of the values of $[[\sigma]]$ (MPa) and $[[\omega^e]]$ (°) given by the FE simulation 3 and those computed from the analytic formulas (bottom).

	A (−40, 0, 0)	B (0,0,0)	C (40,0,0)
$g_{1,1}$	0.00485	0.00080	0.00003
$g_{1,3}$	0.00000	0.00000	0.00000
$\hat{\sigma}_{11}$	20.8	7.1	1.4
$\hat{\sigma}_{22}$	−5.6	−22.2	−21.6
$\hat{\sigma}_{33}$	−58.7	−6.8	0.7
$\hat{\sigma}_{23}$	0.0	0.0	0.0
$\hat{\sigma}_{31}$	0.0	0.0	0.0
$\hat{\sigma}_{12}$	13.3	2.2	−0.3
	FE/Analytic	FE/Analytic	FE/Analytic
$[[\sigma_{11}]]$	565.4/564.2	80.0/78.2	−10.2/−11.5
$[[\sigma_{33}]]$	48.7/47.6	−1.4/−4.0	−9.0/−10.4
$[[\sigma_{31}]]$	0.0/0.0	0/0.0	0.0/0.0
$[[\omega_{32}^e]]$	0.00/0.00	0.00/0.00	0.00/0.00
$[[\omega_{13}^e]]$	0.00/0.00	0.00/0.00	0.00/0.00
$[[\omega_{21}^e]]$	−0.04/−0.06	−0.01/−0.02	−0.01/−0.01

Table 4. Values of $\hat{\sigma}$ (MPa) provided by the FE simulation 4 and used to compute the analytic formulas (28)–(30) and (32) (top). Comparisons of the values of $[[\sigma]]$ (MPa) and $[[\omega^e]]$ (°) given by the FE simulation 4 and those computed from the analytic formulas (bottom).

	A (−40, 0, 0)	B (0, 0, 0)	C (40, 0, 0)
$\hat{\sigma}_{11}$	0.3	0.0	0.0
$\hat{\sigma}_{22}$	0.2	0.2	0.2
$\hat{\sigma}_{33}$	0.2	0.3	0.4
$\hat{\sigma}_{23}$	28.9	29.3	42.1
$\hat{\sigma}_{31}$	7.3	−4.3	−6.4
$\hat{\sigma}_{12}$	−0.1	0.0	0.1

Table 4. Cont.

	FE/Analytic	FE/Analytic	FE/Analytic
$[\sigma_{11}]$	-0.2/-0.1	-0.2/-0.1	-0.2/-0.1
$[\sigma_{33}]$	-0.1/-0.1	0.2/-0.1	-0.2/-0.1
$[\sigma_{31}]$	-10.4/-10.4	-7.4/-7.6	-10.6/-14.1
$[\omega_{32}^e]$	0.00/0.00	-0.01/-0.01	-0.01/-0.01
$[\omega_{13}^e]$	0.00/0.00	0/0	0.00/0.00
$[\omega_{21}^e]$	0.00/0.00	0/0	0.00/0.00

Table 5. Values of $\hat{\sigma}$ (MPa) and ∇g provided by the FE simulation 5 and used to compute the analytic formulas (28)–(30) and (32) (top). Comparisons of the values of $[\sigma]$ (MPa) and $[\omega^e]$ (°) given by the FE simulation 5 and those computed from the analytic formulas (bottom).

	A (-40, 0, 0)	B (0, 0, 0)	C (40, 0, 0)
$g_{3,1}$	0.00455	0.00272	0.00151
$g_{3,3}$	0.00000	0.00000	0.00000
$\hat{\sigma}_{11}$	0.0	-0.2	-0.1
$\hat{\sigma}_{22}$	0.2	0.1	0.1
$\hat{\sigma}_{33}$	0.0	0.1	0.0
$\hat{\sigma}_{23}$	3.5	1.1	1.3
$\hat{\sigma}_{31}$	-4.5	-5.2	-3.9
$\hat{\sigma}_{12}$	0.0	0.0	0.0
	FE/Analytic	FE/Analytic	FE/Analytic
$[\sigma_{11}]$	-0.1/-0.1	0.0/0.0	0.0/0.0
$[\sigma_{33}]$	0.2/0.2	0.2/0.2	0.2/-0.3
$[\sigma_{31}]$	265.8/265.6	161.9/160.2	88.9/87.4
$[\omega_{32}^e]$	0.02/0.03	0.01/0.02	0.00/0.01
$[\omega_{13}^e]$	0.13/0.13	-0.08/-0.08	-0.04/-0.04
$[\omega_{21}^e]$	0.00/0.00	0.00/0.00	0.00/0.00

Table 6. Values of $\hat{\sigma}$ (MPa) and ∇g provided by the FE simulation 6 and used to compute the analytic formulas (28)–(30) and (32) (top). Comparisons of the values of $[\sigma]$ (MPa) and $[\omega^e]$ (°) given by the FE simulation 6 and those computed from the analytic formulas (bottom).

	A (-40, 0, 0)	B (0, 0, 0)	C (40, 0, 0)
$g_{3,1}$	0.00409	0.00230	0.00110
$g_{3,3}$	-0.00002	-0.00001	-0.00002
$\hat{\sigma}_{11}$	-0.2	-0.2	-0.1
$\hat{\sigma}_{22}$	0.2	0.1	0.1
$\hat{\sigma}_{33}$	0.0	0.1	0.0
$\hat{\sigma}_{23}$	4.2	1.5	1.2
$\hat{\sigma}_{31}$	-1.1	0.0	1.6
$\hat{\sigma}_{12}$	0.0	0.0	0.0
	FE/Analytic	FE/Analytic	FE/Analytic
$[\sigma_{11}]$	0.3/-0.1	0.0/0.0	0.0/-0.1
$[\sigma_{33}]$	-0.5/-2.2	-0.3/-0.6	-0.2/-1.8
$[\sigma_{31}]$	239.9/239.9	134.6/133.4	64.9/64.9
$[\omega_{32}^e]$	0.02/0.03	0.01/0.02	0.01/0.01
$[\omega_{13}^e]$	-0.11/-0.11	-0.07/-0.07	-0.03/-0.03
$[\omega_{21}^e]$	0.00/0.00	0.00/0.00	0.00/0.00

Table 7. Elastic parameters for Zn at ambient temperature [22].

$cl a$	C_{11}	C_{33}	C_{44}	C_{12}	C_{13}
1.856	165 GPa	61.8 GPa	39.6 GPa	31.1 GPa	50 GPa

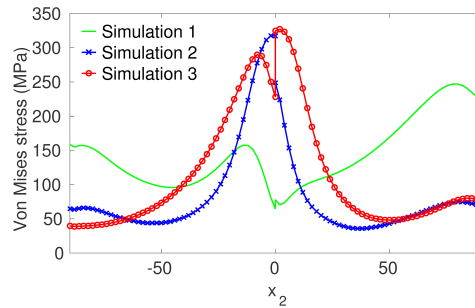


Figure 6. Profiles of Von Mises stress along x_2 through point A $(-40, 0, 0)$ obtained by FE simulations 1, 2 and 3.

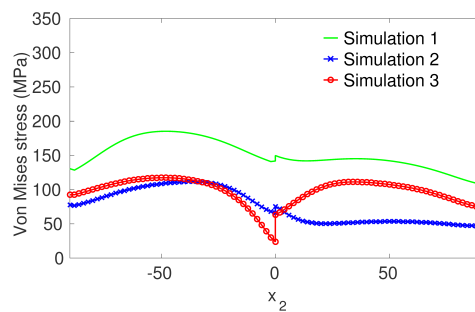


Figure 7. Profiles of Von Mises stress along x_2 through point B $(0, 0, 0)$ obtained by FE simulations 1, 2 and 3.

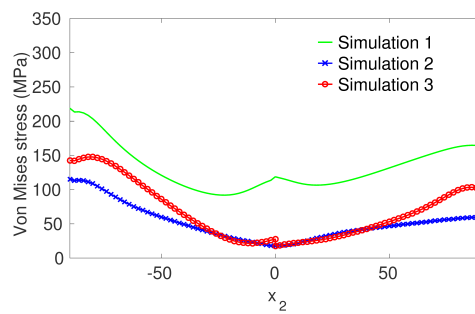


Figure 8. Profiles of Von Mises stress along x_2 through point C $(40, 0, 0)$ obtained by FE simulations 1, 2 and 3.

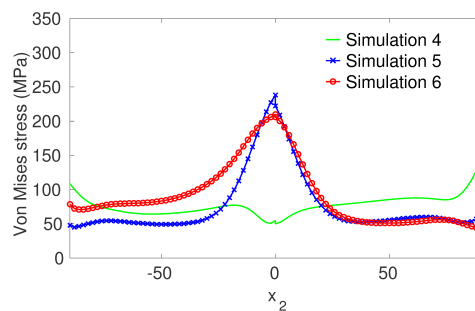


Figure 9. Profiles of Von Mises stress along x_2 through point A $(-40, 0, 0)$ obtained by FE simulations 4, 5 and 6.

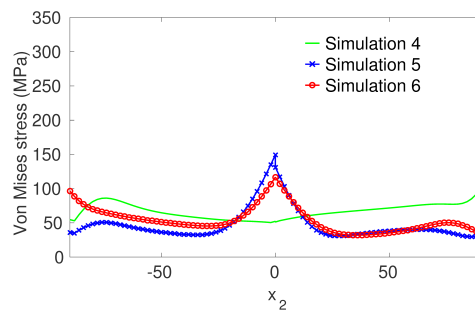


Figure 10. Profiles of Von Mises stress along x_2 through point B (0,0,0) obtained by FE simulations 4, 5 and 6.

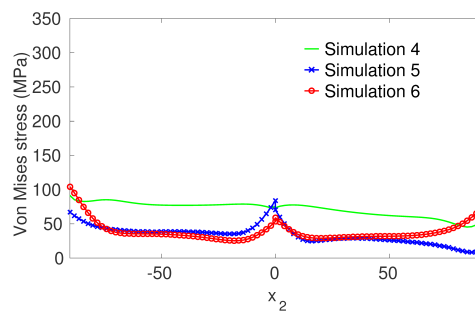


Figure 11. Profiles of Von Mises stress along x_2 through point C (40,0,0) obtained by FE simulations 4, 5 and 6.

4. Discussion

In the absence of plasticity and thermal expansion, source of incompatibilities arise from heterogeneous elasticity and in-plane gradients of GBS which are zero in simulations 1 and 4. Figures 4 and 5 both show that, as one moves away from the pinned line, GBS increases but its gradient decreases. Depending on the shear loading direction and the relative position of the two grains α and β , significant differences in the GBS distribution are however observed. It must be noticed that $[\omega_{13}^e]$ depends only on GBS gradients (Equation (32)) and that incompatibility stresses depend on two terms (Equations (28) and (29)), $\underline{\underline{G}} : (\underline{\underline{[s]}} : \underline{\underline{\hat{\sigma}}})$ due to heterogeneous elasticity and $-\underline{\underline{G}} : \nabla^S \underline{\underline{g}}$ which is related to GBS gradients. Globally, a very good agreement on the jumps of elastic fields is found between the analytic solutions and the values provided by the FE simulations (Tables 1–6), even though the theoretical derivation of the analytic model assumes uniform gradients of $\underline{\underline{g}}$. It seems that the agreement is much better when the contribution of GBS gradients on the elastic field jump increases. As a matter of fact, a perfect match is obtained for all the values of $[\omega_{13}^e]$. Besides, it is noteworthy that, within the present FE configuration, even the fulfillment of the traction vector continuity at the grain boundary is not always perfectly respected.

GBS clearly leads to a relaxation of the main shear stress component in the GB plane: σ_{12} in simulations 2 and 3 to be compared with simulation 1 (Tables 1–3) and σ_{23} in simulations 5 and 6 to be compared with simulation 4 (Tables 4–6). At the same time, as expected from the term $-\underline{\underline{G}} : \nabla^S \underline{\underline{g}}$, incompatibility stresses get more and more pronounced when approaching the pinned line due to growing GBS gradients. This effect is retrieved when looking at the profiles of the Von Mises stress through the GB at different distances from the pinned line (Figures 6–11). Indeed, allowing GBS can induce very strong stress concentrations around GB compared to the case without GBS (Figures 6, 9 and 10) because, in these cases close to the pinned line, the amount of GBS is relatively small and its gradient quite strong. These consequent stresses should then be relaxed by other mechanisms like dislocations glide or climb [2]. On the other hand, far enough from the pinned line, GBS may appear as a relaxation mechanism since the Von Mises stress is much lower with than without GBS in Figures 7, 8 and 11. In these cases, the amount of GBS is relatively high and its gradient has become

almost insignificant. As a consequence, the present simulations emphasize the dual role of GBS which can act both as a strong stress generator and as a stress relaxation mechanism along a same GB. It is important to notice that these effects are shown in the case of a perfectly planar interface with no GBS at the triple line, which is thus different from the GBS accommodation processes discussed in [2,3].

When inverting the positions of grains α and β , the tensor $\underline{\underline{G}}$ is not modified and the signs of GBS gradients remain also unchanged. However, the jump of elastic compliances $[[s]]$ changes sign. Therefore, depending on the relative position of the two grains, the terms $-\underline{\underline{G}} : \nabla^S \underline{g}$ and $\underline{\underline{G}} : ([[s]] : \hat{\sigma})$ may or may not oppose each other, which explains the asymmetry of the results in simulations 2 and 3 and in simulations 5 and 6.

Besides, it is noteworthy that the average stresses across GB are negligible in simulations 5 and 6 ($\hat{\sigma} \simeq 0$ in Tables 5 and 6). It is interesting to underline that a good approximation of the Von Mises stress at GB can then be obtained directly from the analytic terms $-\underline{\underline{G}} : \nabla^S \underline{g}$:

$$\sigma^{VM} \simeq \sqrt{\frac{1}{8} ([[\sigma_{11}]]^2 + [[\sigma_{33}]]^2 + 6[[\sigma_{31}]]^2)} \text{ with } [[\sigma]] \simeq -\underline{\underline{G}} : \nabla^S \underline{g}. \quad (33)$$

For higher values of average stresses across GB, the expression (33) corresponds to a lower bound estimate of the Von Mises stress at GB.

Acknowledgments: The author is grateful to the French National Research Agency (ANR) for financial support under contract “DREAM” (ANR-13-BS09-0001-03).

Conflicts of Interest: The author declares no conflict of interest.

Abbreviations

FE	Finite Element
GB	Grain Boundary
GBS	Grain Boundary Sliding
HCP	Hexagonal Close-Packed

References

- Bell, R.; Langdon, T. An investigation of grain-boundary sliding during creep. *J. Mater. Sci.* **1967**, *2*, 313–323.
- Raj, R.; Ashby, M. On grain boundary sliding and diffusional creep. *Metall. Trans.* **1971**, *2*, 1113–1127.
- Gifkins, R. Grain-boundary sliding and its accommodation during creep and superplasticity. *Metall. Trans. A* **1976**, *7A*, 1225–1232.
- Swygenhoven, H.V.; Derlet, P. Grain boundary sliding in nanocrystalline fcc metals. *Phys. Rev. B* **2001**, *64*, 224105.
- Matsunaga, T.; Kameyama, T.; Ueda, S.; Sato, E. Grain boundary sliding during ambient-temperature creep in hexagonal close-packed metals. *Philos. Mag.* **2010**, *90*, 4041–4054.
- Doquet, V.; Barkia, B. Combined AFM, SEM and crystal plasticity analysis of grain boundary sliding in titanium at room temperature. *Mech. Mater.* **2016**, *103*, 18–27.
- Mussot, P.; Rey, C.; Zaoui, A. Grain boundary sliding and strain compatibility. *Res. Mech.* **1985**, *14*, 69–79.
- Gong, J.; Wilkinson, A.J. Sample size effects on grain boundary sliding. *Scr. Mater.* **2016**, *114*, 17–20.
- Sheikh-Ali, A.; Valiev, R. Effect of plastic incompatibility on grain boundary sliding in zinc bicrystals. *Scr. Metall. Mater.* **1994**, *31*, 1705–1710.
- Martin, G.; Sinclair, C.; Schmitt, J. Plastic strain heterogeneities in an Mg-1Zn-0.5Nd alloy. *Scr. Mater.* **2013**, *68*, 695–698.
- Voigt, W. *Lehrbuch Der Kristallphysik*; B.G. Teubner: Leipzig, Germany, 1928.
- Kosevich, A.M. Crystal dislocations and the theory of elasticity (Chapter 1). In *Dislocations in Solids*; Volume 1; Nabarro, F.R.N., Ed.; North Holland: Amsterdam, The Netherlands, 1979; pp. 33–141.
- Richeton, T.; Berbenni, S.; Berveiller, M. Grain-size dependent accommodation due to intragranular distributions of dislocation loops. *Acta Mater.* **2009**, *57*, 1347–1356.

14. Acharya, A. A model of crystal plasticity based on the theory of continuously distributed dislocations. *J. Mech. Phys. Solids* **2001**, *49*, 761–784.
15. Acharya, A. Constitutive analysis of finite deformation field dislocation mechanics. *J. Mech. Phys. Solids* **2004**, *52*, 301–316.
16. Acharya, A.; Roy, A. Size effects and idealized dislocation microstructure at small scales: Predictions of a Phenomenological model of Mesoscopic Field Dislocation Mechanics: Part I. *J. Mech. Phys. Solids* **2006**, *54*, 1687–1710.
17. Nye, J.F. Some geometrical relations in dislocated crystals. *Acta Metall.* **1953**, *1*, 153–162.
18. Richeton, T.; Berbenni, S. Effects of heterogeneous elasticity coupled to plasticity on stresses and lattice rotations in bicrystals: A Field Dislocation Mechanics viewpoint. *Eur. J. Mech. A Solids* **2013**, *37*, 231–247.
19. Richeton, T.; Tiba, I.; Berbenni, S.; Bouaziz, O. Analytical expressions of incompatibility stresses at $\Sigma 3(111)$ twin boundaries and consequences on single-slip promotion parallel to twin plane. *Philos. Mag.* **2015**, *95*, 12–31.
20. Tiba, I.; Richeton, T.; Motz, C.; Vehoff, H.; Berbenni, S. Incompatibility stresses at grain boundaries in Ni bicrystalline micropillars analyzed by an anisotropic model and slip activity. *Acta Mater.* **2015**, *83*, 227–238.
21. Pérez-Prado, M.; González-Doncel, G.; Ruano, O.; Mcnelley, T. Texture analysis of the transition from slip to grain boundary sliding in a discontinuously recrystallized superplastic aluminium alloy. *Acta Mater.* **2001**, *49*, 2259–2268.
22. Hearmon, R.F. The elastic constants of crystals and other anisotropic materials. In *Landolt-Börnstein Tables, Group III, Volume 11*; Hellwege, K.-H., Hellwege, A.M., Eds.; Springer: Berlin, Germany, 1979; pp. 1–154.



© 2017 by the author. Licensee MDPI, Basel, Switzerland. This article is an open access article distributed under the terms and conditions of the Creative Commons Attribution (CC BY) license (<http://creativecommons.org/licenses/by/4.0/>).